NANO LETTERS

pubs.acs.org/NanoLett Letter

Direct Imaging of Integrated Circuits in CPU with 60 nm Super-Resolution Optical Microscope

Guang Yang,[#] Chi Yang,[#] Yage Chen, Boyu Yu, Yali Bi, Jiangshan Liao, Haozheng Li, Hong Wang, Yuxi Wang, Ziyu Liu, Zongsong Gan, Quan Yuan, Yi Wang,* Jinsong Xia,* and Ping Wang*

Cite This: *Nano Lett.* 2021, 21, 3887−3893 Read Online

ACCESS | Metrics & More | Article Recommendations | Supporting Information

ABSTRACT: Far-field super-resolution optical microscopies have achieved incredible success in life science for visualization of vital nanostructures organized in single cells. However, such resolution power has been much less extended to material science for inspection of human-made ultrafine nanostructures, simply because the current super-resolution optical microscopies modalities are rarely applicable to nonfluorescent samples or unlabeled systems. Here, we report an antiphase demodulation pump−probe (DPP) super-resolution microscope for direct optical inspection of integrated circuits (ICs) with a lateral resolution down to 60 nm. Because of the strong pump−probe (PP) signal from copper, we performed label-free super-resolution imaging of multilayered copper interconnects on a small central processing unit (CPU) chip. The label-free super-resolution DPP optical microscopy opens possibilities for easy, fast, and large-scale electronic inspection in the whole pipeline chain for designing and manufacturing ICs.

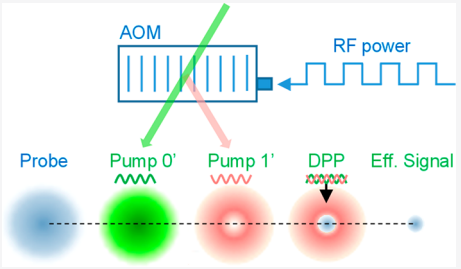

KEYWORDS: *integrated circuit, super-resolution nanoscopy, label-free imaging, far-field imaging, pump−probe*

INTRODUCTION

Semiconductor fabrication has managed to integrate a striking density of nanowires and transistors on a small central processing unit (CPU) chip,[1,2] and the smallest human-made features in CPU quickly reached a nanoscale size inaccessible for inspection by any type of optical microscope. Thus, some expensive tools, such as scanning electron microscopy (SEM), transmission electron microscopy (TEM), and atomic force microscopy (AFM) are routinely implemented, but they are only suited to surface examination of ultrathin samples extracted from a very small part of the entire IC chip. Therefore, the imaging processes have become laborious because of the requirements of a vacuum and time-consuming sample preparation. Current breakthroughs on ptychographic X-ray computed tomography (PXCT)[3] and ptychographic X-ray laminography (PyXL)[4] have successfully achieved nondestructive three-dimensional (3D) imaging of IC chips with a spatial resolution down to 14.6 nm over a large size. However, such an imaging instrument relies on an enormous synchrotron radiation source to supply coherent X-rays, which is usually not accessible for broader applications. Furthermore, the super-resolution optical microscopes have achieved incredible success in revealing nanoarchitectures in single cells.[5−14] However, the human-made semiconductor nanostructures in IC chips have hardly been imaged or characterized by super-resolution optical microscopes because of their inapplicability for fluorescence labeling. Label-free and far-field optical super-resolution nanoscopy was thought to provide tremendous opportunities for direct and easy IC visualization and inspection, and it has also been theoretically and experimentally pursued by various methods in Raman,[15,16] coherent anti-Stokes Raman scattering (CARS),[17−19] stimulated Raman scattering (SRS),[20−26] and pump−probe (PP)[27−29] microscopes. Pump−probe microscopes have demonstrated super-resolution imaging of graphene by applying excessive laser power or higher photon energy in the donut beam to saturate the signal therein.[28,30] Although the pump−probe signal was also observed in copper,[31] the saturation is not applicable to copper wires in ICs. A higher-order CARS microscope has realized super-resolution vibrational imaging of a biological sample.[19] However, CARS could not obtain contrast from copper and other metal materials.

We herein report the antiphase demodulation pump−probe (DPP) microscope and demonstrate direct super-resolution imaging of multilayered copper interconnects in CPU with a lateral resolution down to 60 nm. The copper interconnections exhibit a strong PP response to the intensity modulation of the pump laser. To achieve super-resolution imaging of interweaved copper wires, we impress an additional pump laser in donut shape with antiphase modulation and thus form a modulated subdiffraction-limit focus center (SFC) in the laser focus. We prove the concept by imaging the single-walled carbon nanotube

Received: January 29, 2021
Revised: April 17, 2021
Published: April 27, 2021

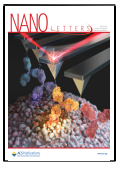

https://doi.org/10.1021/acs.nanolett.1c00403
Nano Lett. 2021, 21, 3887−3893

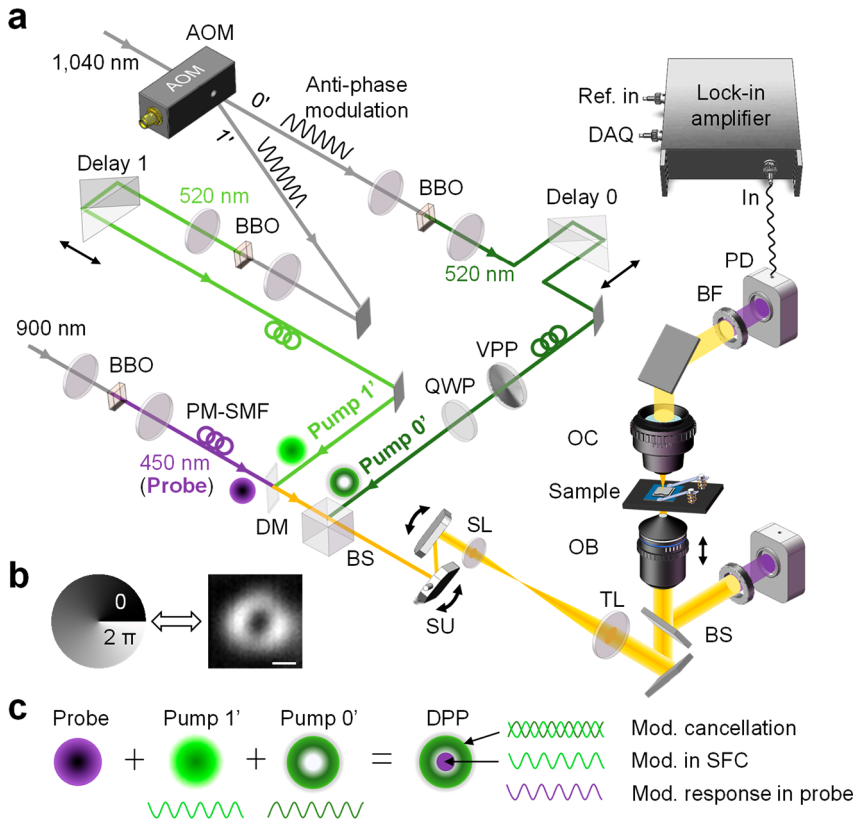

Figure 1. Schematic of DPP microscopy. (a) Experimental schematic of the DPP system. AOM: acousto-optic modulator; VPP: vortex phase plate; QWP: quarter-wave plate; PM-SMF: polarization-maintain single-mode fiber; DM: dichroic mirror; BS: beam splitter; SU: scanning unit; SL: scanning lens; TL: tube lens; OB: objective; OC: oil condenser; BF: bandpass filter; PD: photodiode; ref. in frequency reference from the function generator; DAQ: data acquisition; (b) Phase diagram in VPP and measured donut-shape PSF of the antiphase modulation laser (80 nm gold bead was used). Scale bar, 200 nm. (c) The principle of DPP system. Pump (green), probe (purple), and donut-shaped antiphase modulation lasers are combined and focused on the sample. The probe laser only responds to the modulation in the very center of the Gaussian beam because of the antiphase demodulation in the donut region.

(SWCNT) and boundary artifacts on monolayer graphene. On optical characterization of the CPU chip, we perform super-resolution imaging of the copper interconnects, revealing the fine metal structures with a width of 78 nm. Furthermore, the cross-sectional image depicts the complex metal connections in the CPU from M10 layer down to M1 with details. This in situ label-free super-resolution nanoscopy with specificity of copper provides an optical alternative IC chip inspection.

RESULTS AND DISCUSSION

To achieve ultrahigh sensitivity, laser modulation accompanied by a lock-in amplifier is routinely adopted in the PP microscope. Here, in our concept of DPP super-resolution microscope, counter-phase demodulation is applied in a donut-ring area of the laser focus to achieve a 60 nm imaging resolution. Figure 1a depicts the schematic of the system. After incidence of a 1040 nm femtosecond laser, an acousto-optic modulator (AOM) generated zeroth and first-order diffraction laser beams with automatic counter-phase intensity modulation. Further, two beta-barium-borate (BBO) crystals doubled the frequencies of both beams, and thus, their wavelengths can be reduced in half to 520 nm (pump laser, antiphase modulation laser). To provide independent pulse matching with the probe laser, two time-delay lines were equipped for each of them. To ensure excellent Gaussian beam output and pointing stability, we coupled both lasers into two 0.3-m-long polarization-maintaining single-mode (PM-SM) optical fibers, which not only served as spatial filters but also chirped the femtosecond laser pulses to picosecond pulses. Particularly, one of the collimated 520 nm laser passed through a 2π vortex phase plate (VPP), which converted the Gaussian laser beam to donut shape (Figure 1b). After spatial and temporal combination, the intensity modulation was canceled out in the donut-shaped area and was preserved only in the center of the laser beam. Meanwhile, a 900 nm femtosecond laser was frequency doubled to 450 nm and spatially filtered to serve as the probe laser. The three laser beams were combined and delivered into the microscope by an $X-Y$ scanning galvanometer. A high N.A. objective focused the lasers to the sample with diffraction-limited spot. At the laser focus, the probe laser (indicated in purple in Figure 1c) only responded to the modulation in the very center of the Gaussian beam in the presence of the copper materials and thus allowed subdiffraction-limited super-resolution imaging (see detailed scheme in Supplementary Figure 1).

To experimentally validate the concept and measure the actual spatial resolution of the system, we performed DPP imaging of the single-walled carbon nanotube (SWCNT) and monolayer graphene. The SWCNT is well suited for resolution characterization because a typical SWCNT is about 1−2 nm in diameter and possesses strong PP signal. In Figure 2a,b, we directly compared the PP and DPP images of the SWCNT. DPP allowed significant improvement in lateral resolution, and the full width at half-maximum (fwhm) of the SWCNT was measured to be 60.9 nm (Figure 2c). As shown in Figure 2d,e,

https://doi.org/10.1021/acs.nanolett.1c00403
Nano Lett. 2021, 21, 3887−3893

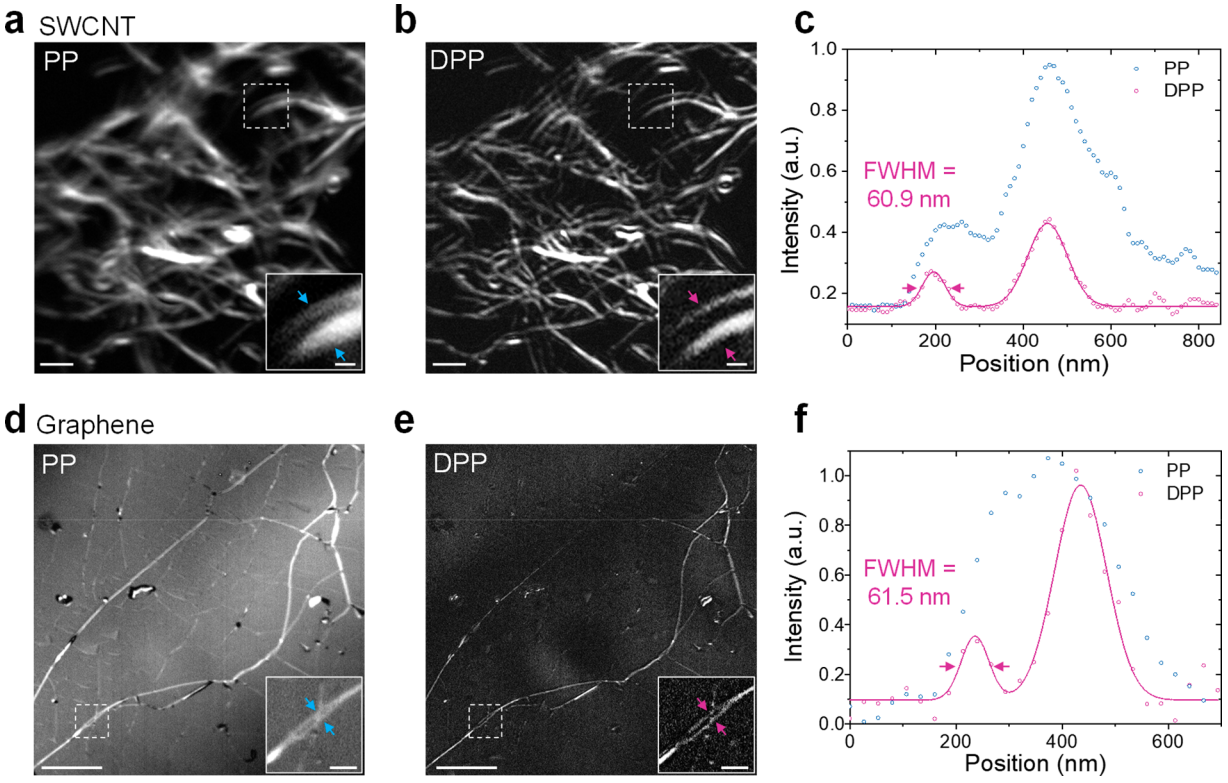

Figure 2. Super-resolution imaging of SWCNTs and graphene. (a,b) PP and DPP images of SWCNTs. Scale bars, 1 μm. Insets are the zoom-in images. Scale bars, 200 nm. (c) Measured intensity profiles of the selected two SWCNTs in (a,b). (d,e) PP and DPP images of the graphene. Scale bars, 5 μm. Zoom-in images are presented in the insets. Scale bars, 1 μm. (f) Measured intensity profiles of the selected pattern in (d,e).

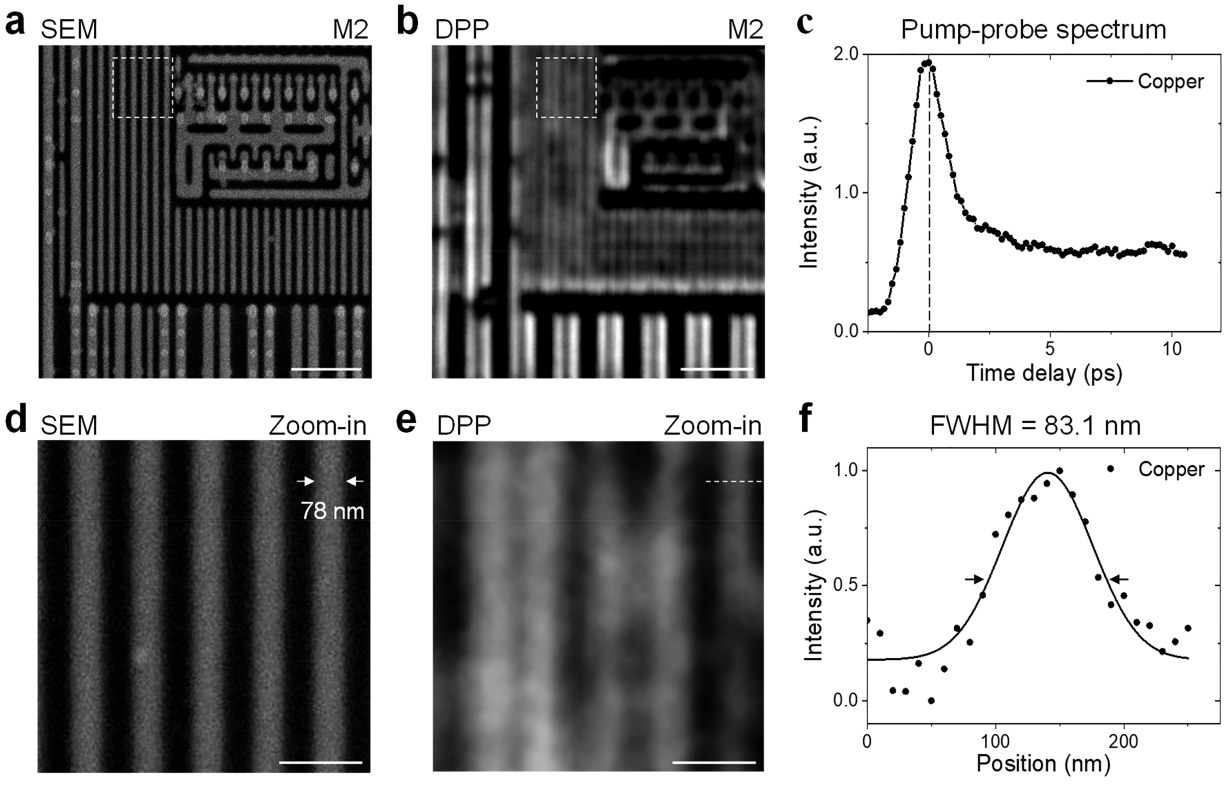

Figure 3. Super-resolution imaging of the M2 layer of a CPU chip. (a,b) SEM and DPP images of the metal layer M2. Scale bars, 1 μm. Note: (a) and (b) compare similar patterns from different locations. (c) PP spectrum obtained from copper wires. (d,e) Zoom-in images corresponding to the boxed regions in (a,b). Scale bars, 200 nm. (f) Measured intensity profile of the selected copper wire indicated by the dashed line in (e).

https://doi.org/10.1021/acs.nanolett.1c00403
Nano Lett. 2021, 21, 3887−3893

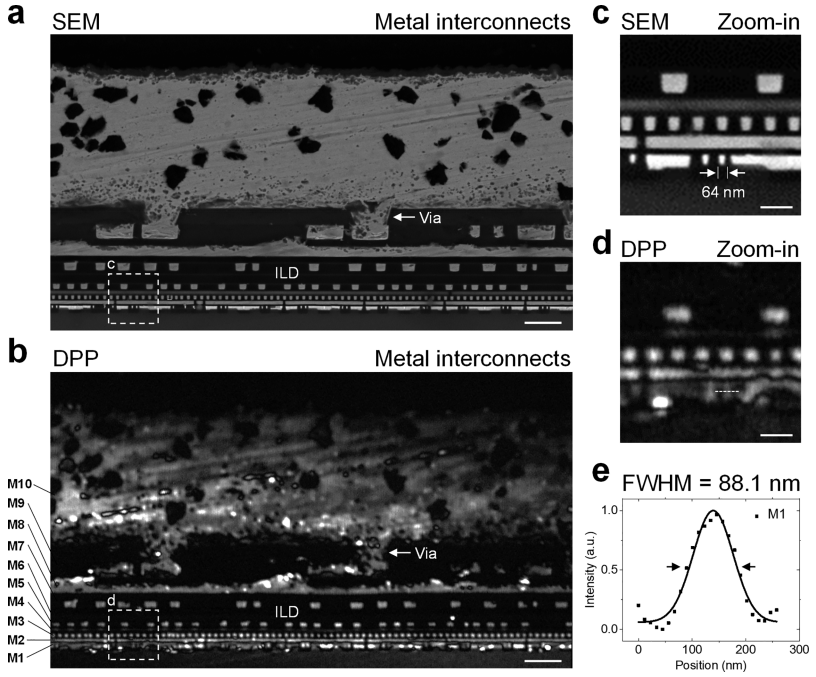

Figure 4. Cross-sectional images of CPU obtained by SEM and DPP. (a,b) Both SEM and DPP images feature the 10 layers of metal interconnects in CPU. Scale bars, 2 μm. (c,d) Zoomed-in images of the indicated part in (a,b), depicting the same degree of accuracy. Scale bars, 500 nm. (e) Measured intensity profile of the selected via in (d).

we further performed super-resolution DPP imaging of nanowrinkles, which are typical artifacts with tens of nm size in monolayer graphene. In contrast to the PP image, the super-resolution DPP image resolved many fine features of these nanowrinkles. In Figure 2f, we plotted and compared the intensity profile of one nanowrinkle as indicated in the boxed area. Additionally, the DPP image displayed the size of the nanowrinkle to be 61.5 nm in fwhm. Because the measured widths of the SWCNT and nanowrinkle are the convolution of the effective point spread function (PSF) of the DPP imaging system and the real size of the SWCNT or nanowrinkle, we evaluated the lateral resolution of our DPP imaging system to be ~60 nm by the measured PSF. Although DPP allows discrimination of very fine features in the sample, weak features become difficult for imaging because of the suppressed signal-to-noise ratio (SNR). As shown in Supplementary Figure 2, the DPP image of the line features with a strong signal present enhanced resolution and maintained good SNR (indicated by the yellow line). However, for weak features appearing in the PP image, the SNR will be significantly suppressed in the super-resolution DPP image.

In semiconductor manufacturing, the engineered multilayer metal interconnection ensures the communications of all electrical components. The copper wires as nanointerconnectors are fundamental to IC chips because of their superior conductivity and low electrical noise. To demonstrate the practical application of the DPP system, we applied it to image nanowires in the commercially available chip, an Intel Core Q8200 processor manufactured with 45 nm technology. The IC was initially prepared by mechanical delayering to the M2 metal layer before imaging. Figure 3 compares the images of the M2 layer obtained by SEM and DPP microscopes. Although SEM provides a higher image quality in Figure 3a, the DPP imaging system not only provides comparable high spatial resolution (Figure 3b) but also measures the time-resolved PP spectrum of copper with femtosecond temporal resolution (Figure 3c). From the zoomed-in view, SEM determined the fwhm of the indicated metal wires to be ~78 nm (Figure 3d). In a similar region, DPP measured the fwhm of the metal wire (Figure 3e) to be 83.1 nm (Figure 3f). Given that the PSF of the DPP system is 60 nm, the optically measured width of the metal wire is consistent with the theoretical prediction (see detailed simulation in Supplementary Figure 3a–d).

Because of the limited space in the chip, metal wires play a vital role in distributing signals, power, and ground vertically. Figure 4a,b compare the cross-sectional images of 10-layer metal interconnects obtained by SEM and DPP. We can clearly identify the tungsten layer on the bottom (M1) and the copper layers on the top (M2–M10). An interlayer dielectric (ILD) functions to electrically separate closely spaced interconnect lines arranged in the different levels. Meanwhile, the vias aid in establishing connections of adjacent copper layers vertically (see detailed data in Supplementary Figure 4a–d). The metal interconnects in the upper layers (M4–M10) possess wider and thicker metal wires to enhance the electrical conductivity and reduce power dissipation. Particularly, the wires in layers from M1–M3 have a size of only about a hundred nanometers, which are indistinguishable for typical optical microscopes. In zoomed-in images shown in Figure 4c,d, we confirmed that the optical DPP can resolve the M1–M3 layers with as much detail as that obtained by SEM. We plot the intensity profile of the indicated via in Figure 4d, and the measured size of it is 88.1 nm in fwhm (Figure 4e). In addition, the DPP super-resolution imaging naturally possesses the capability of optical sectioning attributed to the nonlinear effect. In Supplementary Figure 5a,b, we performed 3D DPP imaging of multiple metal interconnects. Meanwhile, this super-resolution concept can be extended to other imaging methods, such as SRS imaging. As shown in Supplementary Figure 6a, we performed SRS imaging of the optical resist by detecting intrinsic carbon–hydrogen (CH)

https://doi.org/10.1021/acs.nanolett.1c00403
Nano Lett. 2021, 21, 3887–3893

vibrations at 2800−3050 cm^{-1}. The intensity profile of the indicated pattern is presented in Supplementary Figure 6b. The width of the pattern was measured to be 61.7 nm, which is beyond the diffraction limit of the traditional SRS microscope.

SUMMARY

In summary, we have demonstrated the unique potential of DPP microscopy with a spatial resolution of ∼60 nm and super-resolution label-free imaging of SWCNT, graphene, and copper wire interconnections in IC chips. The DPP optical microscopy opens possibilities for easy, fast, and large-scale electronic inspection in the entire pipeline chain of ICs' design, manufacture, and handling defects. Although SEM provides higher imaging resolution, DPP not only provides comparable imaging quality but also enables fast accessibility for broader applications. In particular, the concept of DPP can be extended to SRS microscopy, CARS microscopy, and other fluorescence imaging modalities for significant spatial resolution improvement.

MATERIALS AND METHODS

DPP Microscope. We employed a dual-output femtosecond laser system (InSight DeepSee, Spectra-Physics, Newport) to provide two phase-locked femtosecond lasers with a repetition rate at 80 MHz. The 220 fs output laser at wavelength of 1040 nm was modulated by an acousto-optical modulator (AOM, 1205C-1, Isomet) at 2.3 MHz. The zero-order and first-order diffraction beams automatically possessed opposite modulation phase. To generate shorter laser wavelengths for DPP imaging, we implemented two BBO crystals (4 × 4 × 0.8 mm, SHG@ 1040 nm, Union Optic) to double the frequency of two 1040 nm laser to 520 nm. Similarly, a 100 fs laser at 900 nm was frequency doubled by a BBO crystal (4 × 4 × 0.6 mm, SHG@750−1100 nm, Castech) to 450 nm laser, which served as a probe beam. Two time-delay lines were applied to obtain time-resolved PP spectra. To ensure the three lasers in single mode, we coupled them into three 0.3-m-long optical fibers (PM-S405-XP, Nufern). The demodulation beam passed through the VPP to engineer phase change from 0 to 2π, leading to a doughnut profile. After the pump and probe lasers were spatially overlapped by a dichroic mirror (ZT491dcsp, Chroma Technology) and a 50:50 beam splitter, all lasers were further collinearly delivered into a home-built inverted microscope equipped with a two-axis galvanometer (GVS002, Thorlabs). For super-resolution imaging, we used a high N.A. objective (N.A. 1.49, UAPON 100XOTIRF, Olympus) in all experiments. An objective scanner (P-725.4CD, Physik Instrumente) was installed for 3D imaging. After transmission through the sample, the probe laser was collected by a high N.A. oil condenser (N.A. 1.4, U-AAC, Olympus) and detected by a Si PIN photodiode (S3994-01, Hamamatsu), which is equipped with a 2.3 MHz resonant amplifier. To block the modulated 520 nm laser, two high-quality bandpass filters (ET450/40M/2P, Chroma Technology) were installed in front of the detector. To demodulate the DPP signal, we implemented a high-speed lock-in amplifier (HF2LI, Zurich Instruments) for sensitive heterodyne detection. All imaging signals were acquired by a 1.25 MHz acquisition card (PCI 6251 NI, National Instrument).

In this scheme, an acousto-optic modulator (AOM) plays the key role to generate pump 0′ and pump 1′ lasers with opposite on off states. As the driving radio frequency to the AOM is on (RF ON), ∼ 90% of input laser power will shift to the first order diffraction beam (pump 1′ in the following Supplementary Figure 1). While the RF is turned off (RF OFF), all laser power will return to the zero order of the AOM (pump 0′). Thus, the laser powers of pump 1′ and pump 0′ are always in opposite on/off states depending on the RF power (on or off). The laser power can be balanced and tuned independently by additional wave plates and PBSs. If we turn on/off the RF power at frequency about 2.3 MHz, the pump 0′ and pump 1′ can be modulated in laser intensity but with opposite modulation phase. It means that the intensity modulation will be completely canceled out as the pump 0′ and pump 1′ lasers are spatially overlapped. In our DPP scheme, we intentionally convert the pump 0′ (Gaussian spot) to donut shape by a VPP, and we combined pump 0′ and pump 1′ beams collinearly. Thus, the modulation is canceled out in the donut region and maintained in the center of the laser beam. Therefore, during DPP imaging, we can implement a lock-in amplifier to extract the pump−probe signal responded only at the very center of the probe beam focus and achieve pump−probe imaging of graphene with lateral resolution beyond the diffraction limit.

As the input laser is linearly polarized, the output donut laser focus will become elongated along the polarization direction (see simulation in Supplementary Figure 7).[32] To obtain a symmetric donut shape around the focal point, a quarter waveplate is used to convert linear polarization to circular polarization.

Laser Settings and Data Acquisition. Laser powers were measured at the place between the scan lens and tube lens for all experiments. For SWCNT imaging in Figure 2a,b, the pump, probe and demodulation lasers were set at 450 nm (1 mW) and 520 nm (0.5, 1 mW), respectively. The field of view was 10 × 10 μm^2 with 1000 × 1000 pixels, and the dwell time was 20 μs/pixel. As shown in Figure 2d,e, the field of view in graphene images was 26.5× 26.5 μm^2 with 1000 × 1000 pixels, and the dwell time was 15 μs/pixel. For M2 metal layer imaging in Figure 3b, the pump, probe and demodulation lasers were set at 450 nm (3 mW) and 520 nm (1, 3 mW), respectively. The field of view was 5 × 5 μm^2 with 500 × 500 pixels, and the dwell time was 15 μs/pixel. For the cross-section of metal interconnect layers imaging in Figure 4b and Supplementary Figure 4b,d, the pump, probe and demodulation lasers were set at 450 nm (1.4 mW) and 520 nm (1, 1.3 mW), respectively. The field of view was 16 × 28 μm^2 with 1450 × 2500 pixels, and the dwell time was 40 μs/pixel. SEM imaging was at 7.00 kV in Figure 3a, 4a, and Supplementary Figure 4a. For 3D reconstruction images in Supplementary Figure 5a,b, the field of view was 20 × 20 μm^2 with 2000 × 2000 pixels, and the dwell time was 30 μs/pixel. For optical resist image in Supplementary Figure 6a, the field of view was 15 × 15 μm^2 with 750 × 750 pixels, and the dwell time was 15 μs/pixel.

Samples Preparation for DPP Imaging. *SWCNT.* SWCNT (internal diameter 1−2 nm, XFNANO Materials Technology Co.,Ltd.) and excess sodium dodecyl sulfate (SDS) were dispersed in ethyl alcohol. An ultrasonic pulverizer was used to crush the dispersion for 30 min, and then it was sonicated for 1 h. The suspension was taken after centrifugation at 3000 rpm. The solution of SWCNT was sonicated for 30 min to obtain a homogeneous solution, followed by a 1:1000 dilution with ethyl alcohol.

Graphene. A monolayer graphene sheet (Hefei Vigon Co., Ltd.) grown by chemical vapor deposition (CVD) was transferred onto the silicon waveguide by the wet-transferring method. The graphene film with polymer (poly(methyl

https://doi.org/10.1021/acs.nanolett.1c00403
Nano Lett. 2021, 21, 3887−3893

methacrylate), PMMA) on the top and copper foil on the bottom was floated on the etchant with 10 g of copper sulfate pentahydrate ($CuSO_4 \cdot 5H_2O$), 50 mL of deionized (DI) water, and 50 mL of concentrated hydrochloric acid (HCl). After an etching time of about 1 h, the PMMA/graphene film without copper was transferred into a clean beaker and cleaned with DI water. The chip was dipped into DI water to scoop up the floated PMMA/graphene. Then the sample was baked for 20 min to melt the PMMA resist for better contact between the graphene and waveguides. We put the chip into acetone for 10−15 min to remove the PMMA.

■ ASSOCIATED CONTENT

Supporting Information

The Supporting Information is available free of charge at https://pubs.acs.org/doi/10.1021/acs.nanolett.1c00403.

Details of methods, simulations, and supplementary figures (PDF)

■ AUTHOR INFORMATION

Corresponding Authors

Ping Wang − *Britton Chance Center for Biomedical Photonics, Wuhan National Laboratory for Optoelectronics-Huazhong University of Science and Technology, Wuhan, Hubei 430074, China; MoE Key Laboratory for Biomedical Photonics, Collaborative Innovation Center for Biomedical Engineering, School of Engineering Sciences, Huazhong University of Science and Technology, Wuhan, Hubei 430074, China;* orcid.org/0000-0002-5168-6829; Email: p_wang@hust.edu.cn

Jinsong Xia − *Wuhan National Laboratory for Optoelectronics-Huazhong University of Science and Technology, Wuhan, Hubei 430074, China;* orcid.org/0000-0002-9650-7839; Email: jsxia@hust.edu.cn

Yi Wang − *Wuhan National Laboratory for Optoelectronics-Huazhong University of Science and Technology, Wuhan, Hubei 430074, China*; Email: ywangwnlo@hust.edu.cn

Authors

Guang Yang − *Britton Chance Center for Biomedical Photonics, Wuhan National Laboratory for Optoelectronics-Huazhong University of Science and Technology, Wuhan, Hubei 430074, China; MoE Key Laboratory for Biomedical Photonics, Collaborative Innovation Center for Biomedical Engineering, School of Engineering Sciences, Huazhong University of Science and Technology, Wuhan, Hubei 430074, China*

Chi Yang − *Britton Chance Center for Biomedical Photonics, Wuhan National Laboratory for Optoelectronics-Huazhong University of Science and Technology, Wuhan, Hubei 430074, China; MoE Key Laboratory for Biomedical Photonics, Collaborative Innovation Center for Biomedical Engineering, School of Engineering Sciences, Huazhong University of Science and Technology, Wuhan, Hubei 430074, China*

Yage Chen − *Britton Chance Center for Biomedical Photonics, Wuhan National Laboratory for Optoelectronics-Huazhong University of Science and Technology, Wuhan, Hubei 430074, China; MoE Key Laboratory for Biomedical Photonics, Collaborative Innovation Center for Biomedical Engineering, School of Engineering Sciences, Huazhong University of Science and Technology, Wuhan, Hubei 430074, China;* orcid.org/0000-0002-6601-5198

Boyu Yu − *Britton Chance Center for Biomedical Photonics, Wuhan National Laboratory for Optoelectronics-Huazhong University of Science and Technology, Wuhan, Hubei 430074, China; MoE Key Laboratory for Biomedical Photonics, Collaborative Innovation Center for Biomedical Engineering, School of Engineering Sciences, Huazhong University of Science and Technology, Wuhan, Hubei 430074, China*

Yali Bi − *Britton Chance Center for Biomedical Photonics, Wuhan National Laboratory for Optoelectronics-Huazhong University of Science and Technology, Wuhan, Hubei 430074, China; MoE Key Laboratory for Biomedical Photonics, Collaborative Innovation Center for Biomedical Engineering, School of Engineering Sciences, Huazhong University of Science and Technology, Wuhan, Hubei 430074, China*

Jiangshan Liao − *Britton Chance Center for Biomedical Photonics, Wuhan National Laboratory for Optoelectronics-Huazhong University of Science and Technology, Wuhan, Hubei 430074, China; MoE Key Laboratory for Biomedical Photonics, Collaborative Innovation Center for Biomedical Engineering, School of Engineering Sciences, Huazhong University of Science and Technology, Wuhan, Hubei 430074, China*

Haozheng Li − *Britton Chance Center for Biomedical Photonics, Wuhan National Laboratory for Optoelectronics-Huazhong University of Science and Technology, Wuhan, Hubei 430074, China; MoE Key Laboratory for Biomedical Photonics, Collaborative Innovation Center for Biomedical Engineering, School of Engineering Sciences, Huazhong University of Science and Technology, Wuhan, Hubei 430074, China*

Hong Wang − *Wuhan National Laboratory for Optoelectronics-Huazhong University of Science and Technology, Wuhan, Hubei 430074, China*

Yuxi Wang − *Wuhan National Laboratory for Optoelectronics-Huazhong University of Science and Technology, Wuhan, Hubei 430074, China*

Ziyu Liu − *Wuhan National Laboratory for Optoelectronics-Huazhong University of Science and Technology, Wuhan, Hubei 430074, China*

Zongsong Gan − *Wuhan National Laboratory for Optoelectronics-Huazhong University of Science and Technology, Wuhan, Hubei 430074, China*

Quan Yuan − *Institute of Chemical Biology and Nanomedicine, State Key Laboratory of Chemo/Biosensing and Chemometrics, College of Chemistry and Chemical Engineering, Hunan University, Changsha 410082, China;* orcid.org/0000-0002-3085-431X

Complete contact information is available at: https://pubs.acs.org/10.1021/acs.nanolett.1c00403

Author Contributions

[#](G.Y., C.Y.) These authors contributed equally

Author Contributions

G.Y. and C.Y. carried out the construction of the DPP imaging system. G.Y., Y.G.C., H.W., Y.X.W., Z.Y.Z., and Q.Y. prepared SWCNT, graphene, optical resist, and integrated circuit samples. G.Y. performed experiments. G.Y., P.W., B.Y.Y., and Y.L.B. analyzed the data. G.Y., J.S.L., and H.Z.L. made the simulation. P.W., G.Y., Y.W., J.S.X., and Z.S.G. wrote the manuscript with input from all authors. P.W. and G.Y. conceived the concept. P.W., J.S.X., and Y.W. supervised the project.

Notes

The authors declare no competing financial interest.

The data that support the findings of this study are available from the corresponding authors upon request.

https://doi.org/10.1021/acs.nanolett.1c00403
Nano Lett. 2021, 21, 3887−3893

■ ACKNOWLEDGMENTS

P.W. acknowledges the supports from the National Natural Science Foundation of China 62075076, Science Fund for Creative Research Group of China (61421064), and Innovation Fund of the Wuhan National Laboratory for Optoelectronics.

■ REFERENCES

(1) Gignac, L. M.; Beslin, C.; Gonsalves, J.; Stellari, F.; Lin, C. C. High energy BSE/SE/STEM Imaging of 8 umthick semiconductor interconnects. *Microsc. Microanal.* **2014**, *20* (S3), 8−9.
(2) Orji, N. G.; Badaroglu, M.; Barnes, B. M.; Beitia, C.; Bunday, B. D.; Celano, U.; Kline, R. J.; Neisser, M.; Obeng, Y.; Vladar, A. E. Metrology for the next generation of semiconductor devices. *Nat. Electron.* **2018**, *1* (10), 532−547.
(3) Holler, M.; Guizar-Sicairos, M.; Tsai, E. H. R.; Dinapoli, R.; Müller, E.; Bunk, O.; Raabe, J.; Aeppli, G. High-resolution non-destructive three-dimensional imaging of integrated circuits. *Nature* **2017**, *543*, 402.
(4) Holler, M.; Odstrcil, M.; Guizar-Sicairos, M.; Lebugle, M.; Muller, E.; Finizio, S.; Tinti, G.; David, C.; Zusman, J.; Unglaub, W.; Bunk, O.; Raabe, J.; Levi, A. F. J.; Aeppli, G. Three-dimensional imaging of integrated circuits with macro- to nanoscale zoom. *Nat. Electron.* **2019**, *2* (10), 464−470.
(5) Bates, M.; Huang, B.; Dempsey, G. T.; Zhuang, X. W. Multicolor super-resolution imaging with photo-switchable fluorescent probes. *Science* **2007**, *317* (5845), 1749−1753.
(6) Hell, S. W. Far-field optical nanoscopy. *Science* **2007**, *316* (5828), 1153−1158.
(7) Huang, B.; Jones, S. A.; Brandenburg, B.; Zhuang, X. Whole-cell 3D STORM reveals interactions between cellular structures with nanometer-scale resolution. *Nat. Methods* **2008**, *5* (12), 1047.
(8) Huang, B.; Wang, W. Q.; Bates, M.; Zhuang, X. W. Three-dimensional super-resolution imaging by stochastic optical reconstruction microscopy. *Science* **2008**, *319* (5864), 810−813.
(9) Schmidt, R.; Wurm, C. A.; Jakobs, S.; Engelhardt, J.; Egner, A.; Hell, S. W. Spherical nanosized focal spot unravels the interior of cells. *Nat. Methods* **2008**, *5* (6), 539−544.
(10) Chen, Y. H.; Liu, W. J.; Zhang, Z. M.; Zheng, C.; Huang, Y. J.; Cao, R. Z.; Zhu, D. Z.; Xu, L.; Zhang, M.; Zhang, Y. H.; Fan, J. N.; Jin, L. H.; Xu, Y. K.; Kuang, C. F.; Liu, X. Multi-color live-cell super-resolution volume imaging with multi-angle interference microscopy. *Nat. Commun.* **2018**, *9* (1), 4818.
(11) Tonnesen, J.; Inavalli, V.; Nagerl, U. V. Super-resolution imaging of the extracellular space in living brain tissue. *Cell* **2018**, *172* (5), 1108.
(12) Dong, D.; Huang, X.; Li, L.; Mao, H.; Mo, Y.; Zhang, G.; Zhang, Z.; Shen, J.; Liu, W.; Wu, Z.; Liu, G.; Liu, Y.; Yang, H.; Gong, Q.; Shi, K.; Chen, L. Super-resolution fluorescence-assisted diffraction computational tomography reveals the three-dimensional landscape of the cellular organelle interactome. *Light: Sci. Appl.* **2020**, *9* (1), 11.
(13) Huang, X.; Fan, J.; Li, L.; Liu, H.; Wu, R.; Wu, Y.; Wei, L.; Mao, H.; Lal, A.; Xi, P.; Tang, L.; Zhang, Y.; Liu, Y.; Tan, S.; Chen, L. Fast, long-term, super-resolution imaging with Hessian structured illumination microscopy. *Nat. Biotechnol.* **2018**, *36* (5), 451−459.
(14) Zhao, M. J.; Ye, S.; Peng, X.; Song, J.; Qu, J. L. Green emitted CdSe@ZnS quantum dots for FLIM and STED imaging applications. *J. Innovative Opt. Health Sci.* **2019**, *12* (05), 1940003.
(15) Saito, Y.; Verma, P. Polarization-controlled Raman microscopy and nanoscopy. *J. Phys. Chem. Lett.* **2012**, *3* (10), 1295−300.
(16) Zhou, Y.; Liu, C. H.; Pu, Y.; Wu, B. L.; Nguyen, T. A.; Cheng, G. G.; Zhou, L. X.; Zhu, K.; Chen, J.; Li, Q. B.; Alfano, R. R. Combined spatial frequency spectroscopy analysis with visible resonance Raman for optical biopsy of human brain metastases of lung cancers. *J. Innovative Opt. Health Sci.* **2019**, *12* (02), 1950010.
(17) Dehez, H.; Piché, M.; De Koninck, Y. Resolution and contrast enhancement in laser scanning microscopy using dark beam imaging. *Opt. Express* **2013**, *21* (13), 15912−15925.
(18) Wang, D.; Liu, S.; Chen, Y.; Song, J.; Liu, W.; Xiong, M.; Wang, G.; Peng, X.; Qu, J. Breaking the diffraction barrier using coherent anti-Stokes Raman scattering difference microscopy. *Opt. Express* **2017**, *25* (9), 10276−10286.
(19) Gong, L.; Zheng, W.; Ma, Y.; Huang, Z. W. Higher-order coherent anti-Stokes Raman scattering microscopy realizes label-free super-resolution vibrational imaging. *Nat. Photonics* **2020**, *14* (2), 115.
(20) Gong, L.; Wang, H. Breaking the diffraction limit by saturation in stimulated-Raman-scattering microscopy: A theoretical study. *Phys. Rev. A: At., Mol., Opt. Phys.* **2014**, *90* (1), 10.
(21) Kim, D.; Choi, D. S.; Kwon, J.; Shim, S. H.; Rhee, H.; Cho, M. Selective suppression of stimulated Raman scattering with another competing stimulated Raman scattering. *J. Phys. Chem. Lett.* **2017**, *8* (24), 6118−6123.
(22) Bi, Y.; Yang, C.; Chen, Y.; Yan, S.; Yang, G.; Wu, Y.; Zhang, G.; Wang, P. Near-resonance enhanced label-free stimulated Raman scattering microscopy with spatial resolution near 130 nm. *Light: Sci. Appl.* **2018**, *7*, 81.
(23) Hu, F.; Shi, L.; Min, W. Biological imaging of chemical bonds by stimulated Raman scattering microscopy. *Nat. Methods* **2019**, *16* (9), 830−842.
(24) Ozeki, Y.; Asai, T.; Shou, J.; Yoshimi, H. Multicolor stimulated Raman scattering microscopy with fast wavelength-tunable Yb fiber. *IEEE J. Sel. Top. Quantum Electron.* **2019**, *25* (1), 1.
(25) Ao, J. P.; Feng, Y. Q.; Wu, S. M.; Wang, T.; Ling, J. W.; Zhang, L. W.; Ji, M. B. Rapid, 3D chemical profiling of individual atmospheric aerosols with stimulated Raman scattering microscopy. *Small Methods* **2020**, *4* (2), 1900600.
(26) Wakisaka, Y.; Suzuki, Y.; Iwata, O.; Nakashima, A.; Ito, T.; Hirose, M.; Domon, R.; Sugawara, M.; Tsumura, N.; Watarai, H.; Shimobaba, T.; Suzuki, K.; Goda, K.; Ozeki, Y. Probing the metabolic heterogeneity of live Euglena gracilis with stimulated Raman scattering microscopy. *Nat. Microbiol* **2016**, *1* (10), 16124.
(27) Fathi, A.; Chung, C.-Y.; Lee, Y.-P.; Diau, E. W.-G. Label-free optical microscope based on a phase-modulated femtosecond pump−probe approach with subdiffraction resolution. *ACS Photonics* **2020**, *7* (3), 607−613.
(28) Wang, P.; Slipchenko, M. N.; Mitchell, J.; Yang, C.; Potma, E. O.; Xu, X.; Cheng, J. X. Far-field Imaging of non-fluorescent species with sub-diffraction resolution. *Nat. Photonics* **2013**, *7*, 449−453.
(29) Massaro, E. S.; Hill, A. H.; Grumstrup, E. M. Super-resolution structured pump-probe microscopy. *ACS Photonics* **2016**, *3* (4), 501−506.
(30) Bi, Y.; Yang, C.; Tong, L.; Li, H.; Yu, B.; Yan, S.; Yang, G.; Deng, M.; Wang, Y.; Bao, W.; Ye, L.; Wang, P. Far-field transient absorption nanoscopy with sub-50 nm optical super-resolution. *Optica* **2020**, *7* (10), 1402.
(31) Winter, J.; Rapp, S.; Schmidt, M.; Huber, H. P. Ultrafast laser processing of copper: A comparative study of experimental and simulated transient optical properties. *Appl. Surf. Sci.* **2017**, *417*, 2−15.
(32) Zhan, Q. Chapter 7 - Focusing Through High−Numerical Aperture Objective. In *Three-Dimensional Microfabrication Using Two-photon Polymerization*; Baldacchini, T., Ed.; William Andrew Publishing: Oxford, 2016; pp 168−189.

https://doi.org/10.1021/acs.nanolett.1c00403
Nano Lett. 2021, 21, 3887−3893